Image-based reconstruction of anthropomorphic breast phantoms for synthetic mammogram generation

Computers in Biology and Medicine 198 (2025) 111121

Contents lists available at ScienceDirect

Computers in Biology and Medicine

journal homepage: www.elsevier.com/locate/compbiomed

Image-based reconstruction of anthropomorphic breast phantoms for synthetic mammogram generation

Martina Oria [a,b], Riccardo Ferrero [a], Chiara Andreis [c], Marta Vicentini [a], Ruben van Engen [d], Carlijn Roozemond [d], Paola Lamberti [c], Sara Remogna [c], Alessandra Manzin [a,*]

[a] Istituto Nazionale di Ricerca Metrologica (INRiM), Torino, Italy
[b] Politecnico di Torino, Torino, Italy
[c] Dipartimento di Matematica "Giuseppe Peano", Università degli Studi di Torino, Torino, Italy
[d] Dutch Expert Centre for Screening (LRCB), Nijmegen, Netherlands

ARTICLE INFO

Keywords:
Synthetic mammograms
Breast digital phantoms
X-ray diagnostic imaging
Mammography
In silico modelling
Image acquisition modelling

ABSTRACT

The aim of this work is the generation of realistic synthetic mammograms, using as an input of the imaging acquisition simulation process digital anthropomorphic phantoms, reconstructed from sets of dedicated breast computed tomography (BCT) images from different patients. The voxel-based structure and the segmentation into fibroglandular, adipose and skin tissues are performed through trivariate tensor-product B-spline approximation and morphological operations. The obtained phantoms can be modified by means of geometrical transformations that replicate typical breast shape deformities, and by locally introducing virtual masses and calcifications. After simulating biomechanical compression of the 3D breast phantoms, we generate the mammograms in both craniocaudal (CC) and mediolateral oblique (MLO) views, modelling the x-ray interaction with breast tissues with a Monte Carlo approach implemented in the *in silico* breast imaging pipeline VICTRE.

The methodology proposed here can contribute to the creation of synthetic mammogram databases, to be used for *in silico* testing of diagnostic and therapeutic techniques, as well as for the validation of artificial intelligence (AI) systems in diagnostic imaging and cancer screening. The great advantage is that, from a single BCT scan, it is possible to generate multiple realistic mammograms, with different anatomical features, in terms of breast shape and size, and type and location of lesions.

1. Introduction

Anthropomorphic digital phantoms can be a valuable tool for *in silico* testing and optimization of screening, diagnostic and therapeutic techniques. These enable us to investigate dosimetry implications, as well as how the distribution of tissues and their microstructure can affect the outcomes of different imaging modalities and disease treatments [1–5]. Examples of computational phantoms with realistic anatomical details and high resolution have been developed to support the improvement of diagnostics methods based on magnetic resonance imaging (MRI) [6], ultrasound and photoacoustic imaging [7], x-ray based techniques [8–10], and multi-modal imaging [11]. Moreover, the availability of these tools has enabled the implementation of virtual clinical trials for therapeutic applications, including radiotherapy [12], hyperthermia [13], thermal ablation [14], and surgery [15,16]. To simulate pre-clinical tests and enlarge the spectrum of *in silico* assessment, animal computational models have also been developed besides anthropomorphic phantoms [17], finding applications in both dosimetry and therapeutic technique testing [18–20].

Another important application of 3D digital anthropomorphic phantoms is the generation of synthetic images by means of physical computational modelling, with the scope of enriching existing medical image datasets, which are usually strongly heterogeneous and not sufficiently populated for specific subgroups. This can allow the creation of databases, which can be used for the robust training and accurate validation of artificial intelligence (AI) systems, giving instruments also for explainability tasks. Great efforts have been made in the field of breast imaging, where an invaluable example is the 3D phantom generator integrated in the *in silico* breast imaging simulator VICTRE (Virtual Imaging Clinical Trials for Regulatory Evaluation), designed by Food

* Corresponding author.
E-mail address: a.manzin@inrim.it (A. Manzin).

https://doi.org/10.1016/j.compbiomed.2025.111121
Received 14 April 2025; Received in revised form 17 September 2025; Accepted 19 September 2025
Available online 1 October 2025

and Drug Administration (FDA), to replicate the entire acquisition pipeline of mammography and digital breast tomosynthesis [21]. The VICTRE phantom generator enables to create breasts with different volumes and shapes, including anatomical structures like nipple, ductal tree structure with terminal duct lobular units, glandular compartments, fat and glandular lobules, Cooper's ligament network, and vasculature. To improve realism in tissue texture, advances have been made by deriving the digital breast phantoms from high-resolution 3D clinical breast images, like the ones acquired with the dedicated BCT scanner developed at UC Davis (California, USA). As a fundamental result, a cohort of 150 computerized breast phantoms was generated, to be used for virtual clinical trials in x-ray breast imaging and dosimetry [8]. Different strategies have also been implemented to create a large set of realistic breast phantoms from a relatively small set of BCT data. These include the use of statistical methods exploiting principal component analysis (PCA) [22], or the application of mesh-based geometric transformations and morphing techniques [23].

In this study, we focus on the reconstruction of breast digital phantoms, to be used for the generation of synthetic mammograms with an *in silico* approach that leverages the VICTRE pipeline [21]. The 3D phantoms are derived from clinical BCT images, performing tissue segmentation by means of trivariate tensor-product B-spline approximation [24], in combination with morphological operations. The semi-automatic segmentation and voxel-structure creation are carried out by distinguishing fibroglandular, adipose and skin tissues. To simulate the entire image acquisition process, the phantoms are virtually compressed to a specified thickness, and then used as an input of the Monte Carlo x-ray simulator implemented in VICTRE.

To further enrich the initial dataset and reflect the natural variety of breast morphology and tissue distribution, we modify the original phantoms by (i) applying realistic deformations and (ii) inserting artificial lesions, like masses with well-defined or spiculated margins, and clustered and tubular type calcifications. Synthetic 2D mammograms are then generated in both craniocaudal (CC) and mediolateral oblique (MLO) views. A sample of images is reported, as a proof of the flexibility of the proposed methodology in obtaining, from a low number of reference phantoms, a range of mammograms with large variability in terms of breast shape and size, and type and location of lesions. As a result, from a few sets of BCT images acquired on different patients we can generate 2D mammograms with reduced correlation among each other, and thus useful to expand available datasets for AI system testing and evaluation.

2. Methods

In the following, we describe the entire pipeline for the generation of synthetic mammograms, from 3D breast phantom reconstruction and their geometric transformation up to the x-ray absorption simulation. The implemented methodology, whose steps are depicted in the schematic of Fig. 1, enables us to create a 3D reference phantom from a set of images from one patient undergoing dedicated BCT, after the image conversion into a trivariate B-spline solid. This means that N reference phantoms can be obtained from N sets of BCT images acquired on N patients. The N reference phantoms can be transformed by: (i) applying different types of realistic deformations; (ii) inserting lesions (masses or calcifications) at voxel level. Then, through this procedure we can produce several phantoms differing in shape, volume, tissue composition, and lesion type, position, size and morphology.

2.1. Reference phantom generation

As an input for the generation of 3D reference phantoms, we use dedicated BCT images obtained from a single scan and with a spatial resolution of 273 μm along the three directions. The images were acquired at the Radboud University Medical Center, with a dedicated BCT system from Koning Corporation (West Henrietta, NY, USA), setting the x-ray tube with tungsten target and aluminum filter to a voltage of 49 kV; the first half value layer is 1.39 mm Al, and the nominal focal spot is 0.3 mm [25].

Tissue segmentation is performed on the entire breast volume, which is obtained by combining the BCT slices on the coronal view (yz-plane) from muscle to nipple direction (x-axis) (Fig. 2a). The voxelization and the identification of the main tissues (fibroglandular, adipose and skin tissues) are carried out after applying an imaging operator based on trivariate tensor product B-splines [24], which enable us to visualize the complex texture of breast, and to determine interactively the grey-level

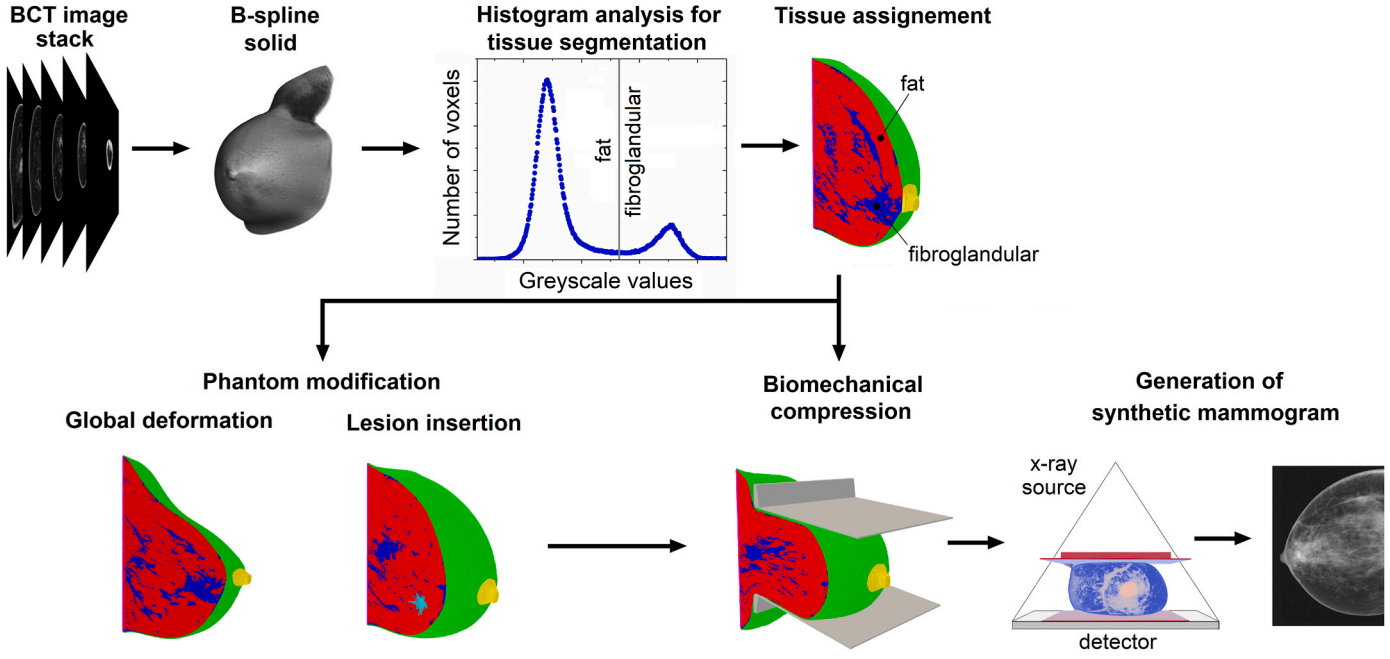

Fig. 1. Schematic of the implemented methodology, including the conversion of one set of dedicated BCT images acquired on one patient into a trivariate B-spline solid, the assignment of tissue properties after greyscale histogram analysis, the phantom transformation via deformation and lesion inclusion at voxel level, its biomechanical compression, and the generation of the synthetic mammogram, from the simulation of the interaction between x-ray and breast tissues.

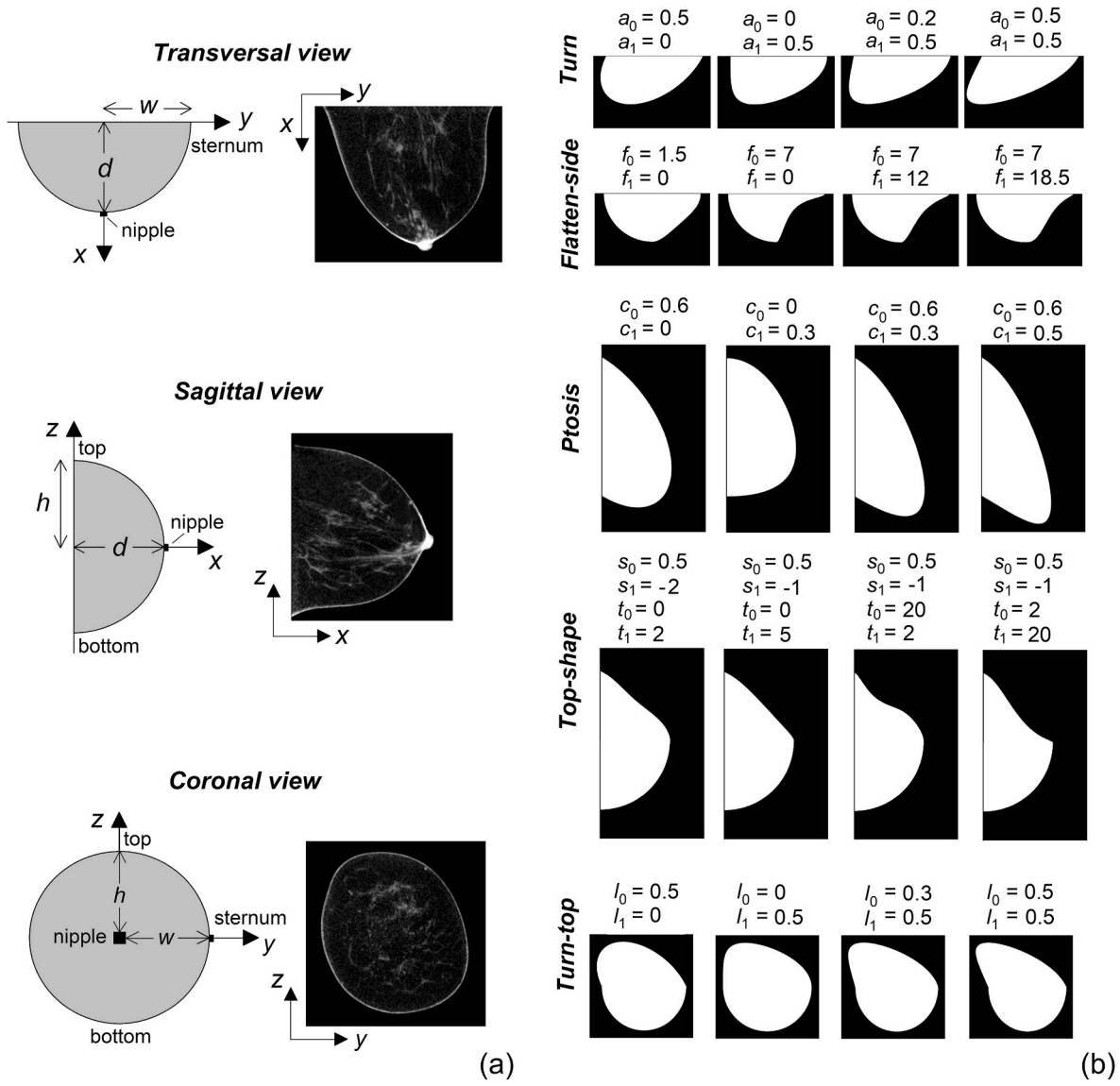

Fig. 2. (a) Schematics of the breast transversal (*xy*), sagittal (*xz*) and coronal (*yz*) planes, with the corresponding BCT slices and the main breast dimensions (i.e. the distance *d* from the torso to the nipple, the width *w* from the centre towards the sternum, and the upper part height *h*). (b) Schematic examples of the effects of the considered deformations when applied to the right breast, for different sets of transformation parameters. In some cases, the considered values are outside the realistic intervals suggested in Table 1, to provide a pictorial idea of the specific role of the parameters on the shape deformation.

thresholds for semi-automatic tissue segmentation. In detail, the discretization in voxels is carried out by introducing a 3D grid with resolution higher than that of the BCT images, described by three knot vectors $\mathbf{U} = \{u_0, u_1, \ldots, u_{n_u+p_u+1}\}$, $\mathbf{V} = \{v_0, v_1, \ldots, v_{n_v+p_v+1}\}$ and $\mathbf{W} = \{w_0, w_1, \ldots, w_{n_w+p_w+1}\}$ along the *u*, *v* and *w* directions. Then, we consider a trivariate B-spline solid of degree (p_u, p_v, p_w), which is a tensor product volume defined as

$$\mathbf{V}(u,v,w) = \sum_{i=0}^{n_u} \sum_{j=0}^{n_v} \sum_{k=0}^{n_w} N_{i,p_u}(u) N_{j,p_v}(v) N_{k,p_w}(w) \mathbf{P}_{ijk}. \quad (1)$$

In Eq. (1), $\mathbf{P}_{ijk}$ ($i = 0, 1, \ldots, n_u$, $j = 0, 1, \ldots, n_v$, $k = 0, 1, \ldots, n_w$) are the control points, and $N_{i,p_u}(u)$, $N_{j,p_v}(v)$ and $N_{k,p_w}(w)$ are the univariate B-spline basis functions, constructed on the knot vectors **U**, **V** and **W**, and with degree p_u, p_v and p_w, respectively. In our model, we assume that the *u*, *v* and *w* directions are parallel to the Cartesian axes previously introduced, and $p_u = p_v = p_w = 2$ (i.e., triquadratic B-splines are considered).

After the generation of the trivariate B-spline solid and of the corresponding discretized volume with cubic voxels of 109 μm size, the graphic visualization of the associated B-spline surfaces is exploited for adipose tissue segmentation, in combination with histogram analysis. The aim is to identify the grey-level threshold below which we assign the corresponding voxels to fat. Then, we extract the skin layer by means of a radial-geometry edge detection scheme applied to each coronal section with thickness equal to voxel size, deriving a mean breast skin thickness around 1.5 mm [26]. With this segmentation procedure, we prevent the inclusion of regions adjacent to the inner skin boundary with similar grey levels, like blood vessels. After the application of a morphological erosion operation to the skin layer, we assign the remaining voxels to fibroglandular tissue, including vasculature and possible muscle region. Then, we re-add the skin, varying the maximum number of voxels adjoined along radial directions, in order to obtain phantoms with different skin thickness.

The pectoralis muscle is usually not included in dedicated BCT images and CC view mammograms, while a significant portion of it typically appears in MLO view mammograms. This requires modifying the obtained breast phantoms specifically for the MLO projection, by

properly incorporating the pectoralis muscle from the armpit down to the posterior nipple line. To this aim, a paraboloid with an ellipsoidal cross-section and axis parallel to the projection direction is superimposed onto the posterior region of the phantom. In the overlapping area, the original tissue is replaced with muscle tissue. To soften the transition at tissue interface, the muscle surface is slightly eroded, blurring the edges created by the Boolean operation. Additionally, the phantom is extended towards the sternum to accommodate the compression of a larger portion of the breast, including the muscle. This extension remains outside the compression paddles and does not appear in the image, serving solely to provide the necessary thickness for realistic breast compression.

2.2. Global deformation application

Geometric transformations are applied to the reference phantom, replicating realistic deformities that can be observed in breast shape. The geometrical structure is altered by shifting voxels from their original positions to new positions without modifying the tissue assignment. The data are then interpolated on the input regular grid, with the nearest-neighbour approach.

Following Ref. [27] we consider: (i) turn deformation, occurring when the breast points towards the external flank; (ii) flatten-side deformation, describing the flattening of the breast towards the sternum; (iii) ptosis, which models sagging effects; (iv) top-shape deformation, which simulates variations in concavity of the breast top half; (v) turn-top deformation, occurring when the breast top half turns towards the shoulder. The transformations are expressed as a function of the main breast dimensions shown in Fig. 2a, i.e. the distance from the torso to the nipple for the x-axis direction (d), the width from the centre towards the sternum for the y-axis direction (w), and the upper part height or maximum length from the centre towards the clavicle for the z-axis direction (h). To obtain realistic deformations of the breast shape, the relevant parameters of each transformation should be approximately varied within the ranges listed in Table 1, where we have also indicated the interested plane and the views on which the specific transformation produces a visible effect.

Turn deformation, which is responsible for the breast bending towards the body lateral part, can be described by scaling the lateral position (y) of a point versus its distance (x) from the torso, as:

$$\begin{aligned} x' &= x \\ y' &= y - w\left[a_0\left(\frac{x}{d}\right) + a_1\left(\frac{x}{d}\right)^2\right] \\ z' &= z \end{aligned} \quad (2)$$

The turn towards the external flank can be modelled by assigning positive values to parameters a_0 and a_1 in the case of the right breast, while negative values have to be considered for the left breast. Realistic deformations can be obtained by varying the absolute values of a_0 and a_1 within the ranges 0−0.3 and 0−0.5, respectively, as reported in Table 1.

Flatten-side deformation produces a compression of the internal part of the breast, transforming only the points with $y > 0$ for the right breast, and with $y < 0$ for the left breast. This can be described by modulating the x-coordinate of a point versus its lateral position y, as:

$$\begin{aligned} x' &= xf(y) = x\left[b_3\left(\frac{y}{w}\right)^3 + b_2\left(\frac{y}{w}\right)^2 + b_1\left(\frac{y}{w}\right) + b_0\right] \\ y' &= y \\ z' &= z \end{aligned} \quad (3)$$

Parameters b_i ($i = 0$−3) can be derived by imposing the following constraints on function $f(y)$:

$$\begin{aligned} f(0) = 1,\ f(w) = f_0 \\ f'(0) = 0,\ f'(w) = f_1 \end{aligned}, \quad (4)$$

where f_0 and f_1 control the flattening in correspondence of the sternum and breast middle part, respectively. It results: $b_3 = f_1 + 2 - 2f_0$, $b_2 = -f_1 - 3 + 3f_0$, $b_1 = 0$, $b_0 = 1$. Realistic deformations can be obtained by varying f_0 and f_1 within the ranges 1.5−5 and 0−$f_0^{3/2}$, respectively (Table 1); no deformations are introduced when $f_0 = 1$ and $f_1 = 0$.

Ptosis deformation, which causes breast drooping, can be simulated by modifying the vertical position (z) of a point as a function of its distance (x) from the torso, according to:

$$\begin{aligned} x' &= x \\ y' &= y \\ z' &= z - h\left[c_0\left(\frac{x}{d}\right) + c_1\left(\frac{x}{d}\right)^2\right] \end{aligned} \quad (5)$$

Realistic deformations can be simulated by changing parameters c_0 and c_1 within the ranges 0−0.6 and 0−0.3, respectively (Table 1).

Top-shape deformation, which produces a modification of the curvature of the upper part of the breast, can be described by scaling the z-coordinate of a point (if $z > 0$) versus its x position, as:

$$\begin{aligned} x' &= x \\ y' &= y \\ z' &= zg(x) = z\left[e_5\left(\frac{x}{d}\right)^5 + e_4\left(\frac{x}{d}\right)^4 + e_3\left(\frac{x}{d}\right)^3 + e_2\left(\frac{x}{d}\right)^2 + e_1\frac{x}{d} + e_0\right] \end{aligned} \quad (6)$$

Parameters e_i ($i = 0$−5) can be derived by imposing the following constraints on function $g(x)$:

Table 1
List of breast geometrical transformations with the indication of the interested plane, the affected views and the interval of variations of the parameters leading to realistic deformations.

Geometrical transformation	Interested plane		Affected views	Parameter ranges	
				Right breast	Left breast
Turn deformation	xy		CC	$0 \le a_0 \le 0.3$	$-0.3 \le a_0 \le 0$
				$0 \le a_1 \le 0.5$	$-0.5 \le a_1 \le 0$
Flatten-side deformation	xy	$y > 0$ (right) $y < 0$ (left)	CC	$1.5 \le f_0 \le 5$ $0 \le f_1 \le f_0^{3/2}$	$1.5 \le f_0 \le 5$ $0 \le f_1 \le f_0^{3/2}$
Ptosis deformation	xz		MLO	$0 \le c_0 \le 0.6$ $0 \le c_1 \le 0.3$	$0 \le c_0 \le 0.6$ $0 \le c_1 \le 0.3$
Top-shape deformation	xz ($z > 0$)		MLO	$0 \le s_0 \le 0.5$ $-2 \le s_1 \le -1$ $0 \le t_0 \le 20$ $2 \le t_1 \le 15$	$0 \le s_0 \le 0.5$ $-2 \le s_1 \le -1$ $0 \le t_0 \le 20$ $2 \le t_1 \le 15$
Turn-top deformation	yz ($z > 0$)		CC, MLO	$0 \le l_0 \le 0.3$ $0 \le l_1 \le 0.5$	$-0.3 \le l_0 \le 0$ $-0.5 \le l_1 \le 0$

$$\begin{matrix} g(0)=1,\ g(d)=1 \\ g'(0)=s_0,\ g'(d)=s_1 \\ g''(0)=t_0,\ g''(d)=t_1 \end{matrix} \quad , \tag{7}$$

where s_0 and s_1 are the slope parameters at the torso and nipple, respectively, while t_0 and t_1 are the relative curvature parameters. It results:

$$\begin{matrix} e_5=-\frac{1}{2}t_0-3s_0-3s_1+\frac{1}{2}t_1,\ e_4=\frac{3}{2}t_0+8s_0+7s_1-t_1, \\ e_3=-\frac{3}{2}t_0-6s_0-4s_1+\frac{1}{2}t_1,\ e_2=\frac{1}{2}t_0,\ e_1=s_0,\ e_0=1 \end{matrix} \quad . \tag{8}$$

Realistic deformations can be obtained by varying parameters s_0, s_1, t_0 and t_1 within the ranges reported in Table 1.

Turn-top deformation, which modifies only the upper part of the breast ($z>0$) producing again a lateral bending as turn deformation, can be simulated by varying the y-coordinate of a point versus its vertical position z, as:

$$\begin{matrix} x'=x \\ y'=y-w\left[l_0\left(\frac{z}{h}\right)+l_1\left(\frac{z}{h}\right)^2\right] \\ z'=z \end{matrix} \quad . \tag{9}$$

To model realistic deformations, the absolute values of parameters l_0 and l_1 should be varied within the intervals 0−0.3 and 0−0.5, respectively (Table 1). Positive values have to be assigned in the case of the right breast, while negative values have to be considered for the left breast.

To give a pictorial description of the effects of the considered deformations, Fig. 2b reports a list of images showing the modifications of a schematized section of the right breast in the plane involved in the transformation, for different selections of the parameter set. Values outside the realistic intervals suggested in Table 1 are also considered, to better highlight the geometric transformation effects.

2.3. Synthetic image generation

For generating the synthetic mammograms from the 3D breast phantoms, we first compress the phantoms, after having added a few slices of muscle to the more internal coronal slice, by means of the finite element biomechanics solver FEBio integrated in VICTRE [28]. This enables us to model the compression phase, once specified the target thickness, which is defined on the basis of the percentage of fibroglandular tissue. To fix the breast compression thickness, we refer to the volumetric breast density grade scores proposed by Volpara® and correlated to the visual BI-RADS® 5th edition density categories [29,30]. For the derivation of the mammograms in CC view, the compression is simulated by positioning the breast between two horizontal rigid plates parallel to the xy-plane, while for the MLO view the two parallel plates are rotated 45°.

The compressed phantoms are then used as an input to the Monte Carlo x-ray solver integrated in VICTRE, which enables us to obtain both the “for processing” and “for presentation” images, reproducing the image processing of the Siemens Mammomat Inspiration system. According to Ref. [21], the x-ray energy spectrum is sampled from a pre-computed probability distribution function corresponding to a 28 kVp tungsten anode source with a 50 μm rhodium filter and a 1 mm beryllium window [31]. A 200 μm thick amorphous selenium direct-conversion detector, with 85 μm resolution, is simulated, including a 1 mm thick protective cover and a focused anti-scatter grid with parallel strips. The distance between the x-ray source and the detector is fixed to 65 cm. The calculation of the x-ray projection is performed by setting the mass density of fat, fibroglandular tissue, added muscle and skin plus nipple at 0.92, 1.035, 1.05 and 1.09 g/cm^3, respectively; for masses we fix the density to 1.2 g/cm^3, and for calcifications to 1.8 g/cm^3 [32,33].

It is important to point out that despite the produced mammograms contain 85 μm pixels, these are acquired on phantoms with 109 μm sized voxels, derived from BCT images with 273 μm resolution. This means that the synthetic images inherit the low resolution of the source data, with the limitation that fine-scale features cannot be well depicted.

3. Results and discussion

In the following, the methodology described in Section 2 is applied to generate a sample of synthetic mammograms, with different breast shape, size, tissue composition, and type of lesion. To this aim, we consider four sets of dedicated BCT images acquired on four patients, which enable us to produce four reference phantoms, independent from each other in terms of tissue composition.

3.1. Reference phantom generation and synthetic mammogram acquisition

The reference phantom construction is depicted in Fig. 3, for a stack of dedicated BCT images acquired on a specific patient, here named patient #1. By combining the BCT slices on the coronal view, we obtain a 3D grid of 624 × 592 × 243 pixels, with size of 273 μm. A trivariate triquadratic B-spline solid is then built using the 3D grid to produce a digital phantom, composed of 109 μm cubic voxels with associated grey levels. The tissue classification is performed by analysing the histogram of the overall grey levels obtained after B-spline approximation. This is shown in Fig. 3a, together with the Gaussian fit, the residual histogram, derived by subtracting the Gaussian fitting curve, and the Gaussian fit of the residual. From the comparison of the two peaks amplitude and width, it is possible to determine the tissue composition, considering that the interval in Hounsfield units for fat typically ranges from −200 to −50 HU [34,35]. For the specific breast here examined, the peak with the largest amplitude and width, corresponding to fat, is located at −173 HU, and we define a threshold of −135 HU to separate it from fibroglandular tissue; then, we identify the skin layer. The tissue distribution calculated slice-by-slice along the x-direction, from the thorax muscle to the nipple, is reported in Fig. 3b. Globally, when the full skin layer is considered, the phantom volume is composed of 85 % fat, 11 % fibroglandular tissue and 4 % skin (including the nipple region). Within the category of fibroglandular tissue we also include vasculature and muscle, having similar mass density and thus comparable x-ray attenuation for synthetic mammogram generation. The top, side and front views of the obtained right breast phantom, used as a reference for the transformations reported in Sub-sections 3.2 and 3.3, are depicted in Fig. 3c, together with a sagittal section representing the tissue internal distribution, corresponding to a heterogeneously dense breast (Fig. 3d). The main phantom dimensions, as defined in Sub-section 2.2, result to be d = 9.5 cm, w = 5.3 cm and h = 5.6 cm.

According to the volumetric breast density grade scores proposed by Volpara® and considering the specific percentage in volume of fibroglandular tissue (11 %) found in the constructed phantom, we opt for a breast compression thickness of 6 cm for the calculation of the x-ray projections [36,37]. The synthetic mammograms, generated in the “for presentation” form, are reported in Fig. 4a for the CC view and in Fig. 4b for the MLO view. In order to simulate skin loss, which can occur in real digital mammograms, due to image saturation above a specific x-ray exposure [38], the images are derived for different skin thicknesses, from less (0.109 mm) to more (1.090 mm) realistic values.

It is important to note that, in addition to the projection related to the different tissue attenuation coefficients, the derivation of “for presentation” images in VICTRE pipeline requires the calculation of the projection of a homogeneous phantom, with the same shape and voxel decomposition of the original 3D breast phantom but entirely made of adipose tissue. In such a way, it is possible to obtain a map that allows us to identify the regions of the breast with reduced thickness along the

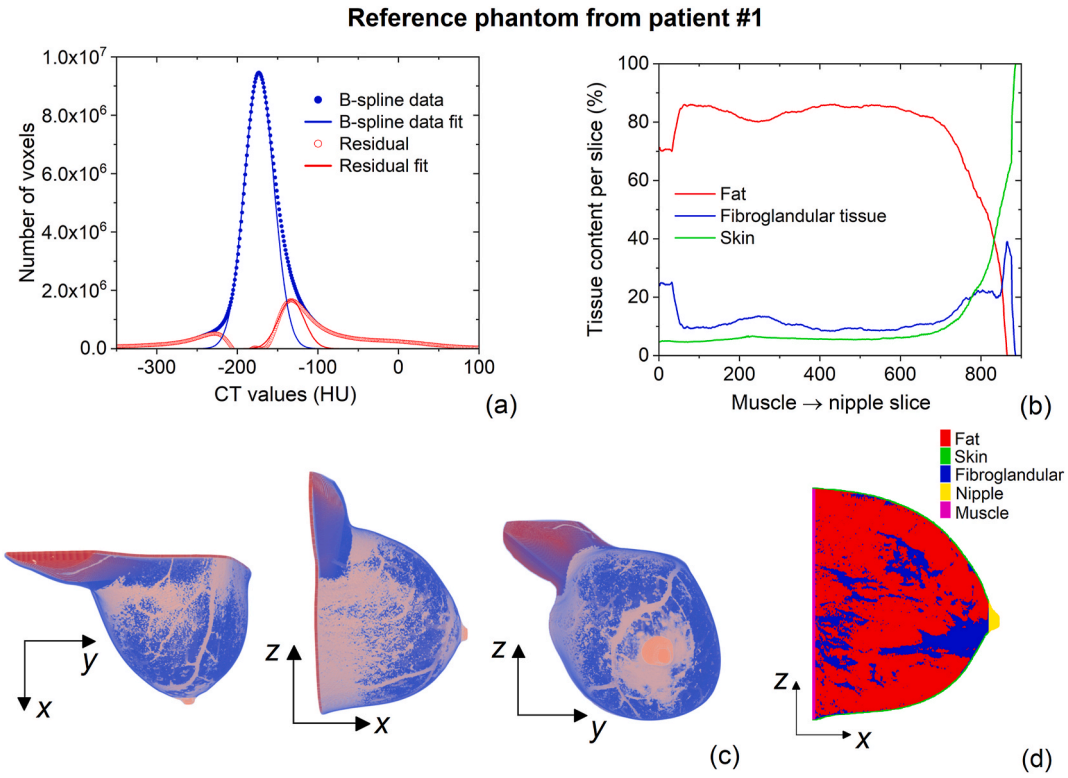

Fig. 3. (a) Histogram of the overall grey levels obtained after B-spline approximation of the set of dedicated BCT images from patient #1, used for the choice of the threshold for the classification of fat and fibroglandular tissues. The graph also contains the relative Gaussian fit, the residual histogram, derived by subtracting the Gaussian fit curve, and the Gaussian fit of the residual. (b) Percentages of fat, fibroglandular and skin tissues per each coronal slice from muscle to nipple. (c) Transversal (left), sagittal (centre) and coronal (right) views of the obtained reference breast phantom. (d) Phantom section on median sagittal plane (*xz*), with the spatial distribution of the different considered tissues.

compression direction, like the skin. Then, the "for presentation" image is calculated by multiplying the grey level at each pixel in the original projection by the inverse of the greyscale value of the corresponding pixel in the homogeneous phantom projection. This process enables us to clearly visualize the total skin edge, which appears as a thick light grey line that follows the entire breast boundary, when the input skin thickness is within the normal range, i.e. 0.7−2.3 mm [39]. To obtain mammograms more similar to the real ones, where the skin is not so evident and resolution artefacts are present at the breast boundary, we opt for a decrease in the skin thickness down to 0.545 mm, reducing the number of skin voxel layers to 5. This value is selected for the following modelling analysis.

To demonstrate the application of the methodology in different cases, Fig. 5 shows the results obtained on other three sets of BCT images acquired on three different patients, illustrating, on the left, the original BCT images compacted in 3D objects, in the centre, the percentages of main tissues per each coronal slice from muscle to nipple, extracted from trivariate B-spline solids, together with the reconstructed reference phantoms, and, on the right, the calculated mammograms in CC view. The derived phantoms differ in size, being about $11.4 \times 12.7 \times 15.1$ cm^3 for patient #2, $8 \times 9.2 \times 11.5$ cm^3 for patient #3, and $10 \times 12 \times 14.8$ cm^3 for patient #4. These have a variable percentage of fibroglandular tissue, whose segmentation is performed after fixing the thresholds below which we assume to have fat. After histogram analysis, the selected values are −115 HU, −45 HU and −115 HU, for the phantoms of patients #2, #3 and #4, respectively. Following this choice, phantoms from patients #2 and #3 contain a percentage of fibroglandular tissue of 17 % and 21 %, respectively, thus according to Volpara® volumetric density grade scores they belong to the class of extremely dense breasts; for them, we opt for a compression of 5 cm. Phantom from patient #4 is composed of 15 % fibroglandular tissue and can be associated with the class of heterogeneously dense breasts; this is compressed to 5.5 cm. The generated mammograms reflect the variability in tissue composition, with the ones acquired on phantoms #2 and #3 characterized by high density areas distributed throughout the breast shape, and the fourth one interested by a more compacted fibroglandular region.

3.2. *Application of geometrical transformations*

Starting from the reference phantoms previously reconstructed (see Figs. 3 and 5), we can generate multiple synthetic mammograms in both CC and MLO views, by simply applying the geometrical transformations described in Sub-section 2.2. To obtain realistic deformations of the breast shape, the relevant parameters of each transformation should be approximately varied within the ranges listed in Table 1. It is clear that by properly setting the transformation parameters, it is possible to obtain a large number of digital phantoms and thus synthetic mammograms. Some examples are shown in Fig. 6 for the reference breast phantom #1, distinguishing between the transformations that produce shape variations mainly visible in a specific view (CC or MLO) and in both. The shape modifications can be appreciated by comparing the deformed phantoms depicted on the top of Fig. 6 to the transversal, sagittal and coronal views of phantom #1 in Fig. 3c.

Focusing on the transformations responsible for breast shape modifications in the transversal planes and thus observable in CC view, the images shown in Fig. 6a are obtained for turn deformation by setting parameters a_0 and a_1 at 0.001 and 0.47, and for flatten-side deformation by fixing $f_0 = 2.5$ and $f_1 = 4.5$. By comparing these mammograms to the ones in Fig. 4a, it is well evident how the turn deformation is responsible for a more pronounced breast curvature at the external side, which can be incremented by increasing parameter a_0. On the contrary, the flatten-

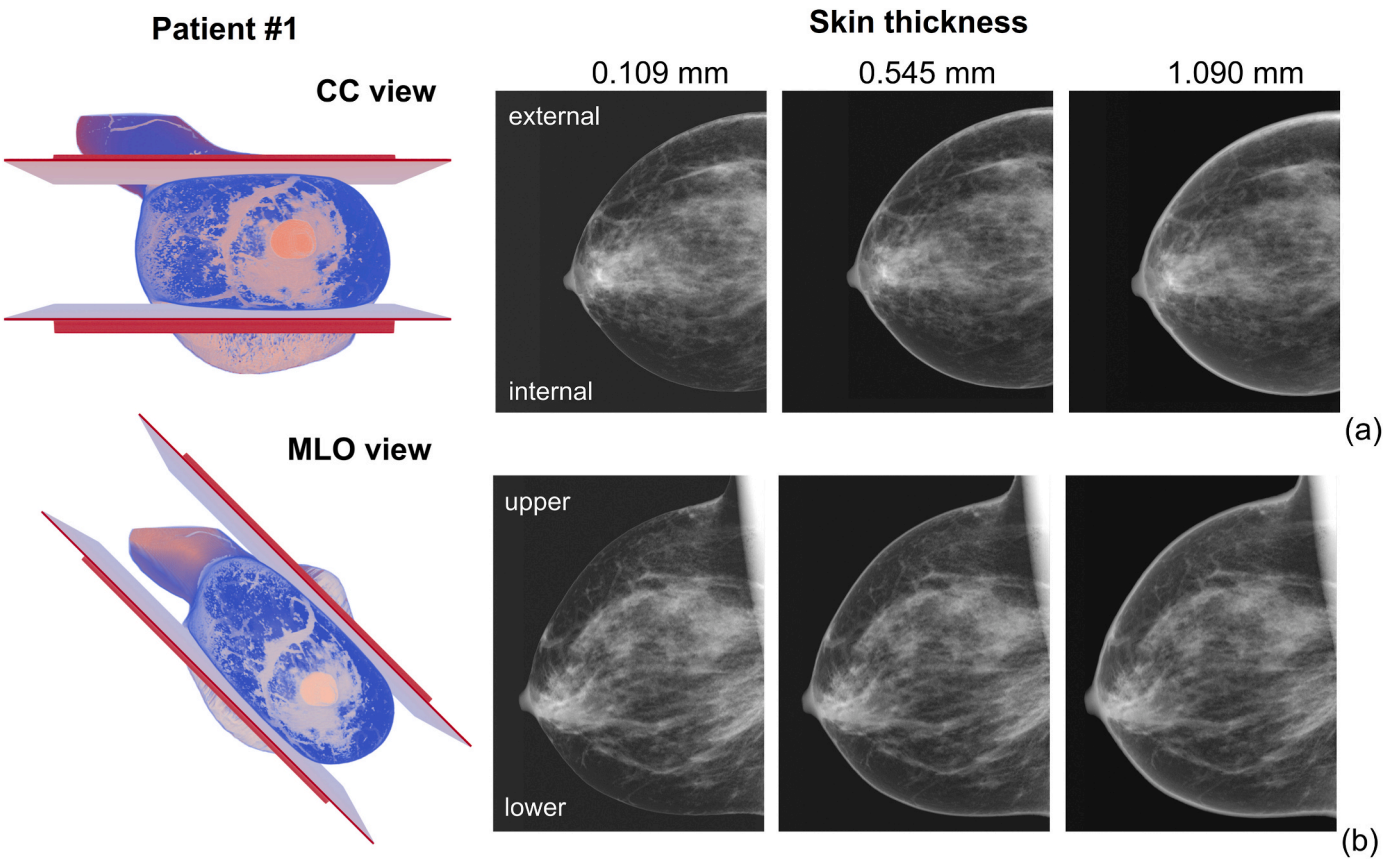

Fig. 4. Visualization of the biomechanical compression of the reference breast phantom from patient #1 and synthetic mammograms generated with skin thickness variable from 0.109 to 1.090 mm, for (a) craniocaudal (CC) and (b) mediolateral oblique (MLO) views.

side causes a compression of the internal part, which can be amplified for higher values of f_0.

Considering the transformations that lead to sagittal plane variations and thus detectable in MLO view, the images in Fig. 6b are derived by setting $c_0 = 0.6$ and $c_1 = 0.15$ for ptosis, and $s_0 = 0.1$, $s_1 = -2$, $t_0 = 20$ and $t_1 = 3$ for top-shape deformation. In the first case, a strong modification of the breast profile is produced with respect to the images shown in Fig. 4b, with a noticeable hanging down effect, which can be further raised by increasing c_1. In the second case a compression of the top part is obtained, with a curvature variation, which can be made more pronounced for higher values of t_1.

Finally, the effects of turn-top deformation, which contributes to modifications in the coronal planes, are depicted in Fig. 6c, for both CC and MLO images, obtained with $l_0 = 0.175$ and $l_1 = 0.2$. Even if this deformation produces a significant deflection of the top-half of the breast towards the external side, the obtained mammograms result to be very similar to the reference phantom ones, due to the negligible profile variations on the projection planes, for both CC and MLO views.

Additional phantoms and relative synthetic mammograms can be obtained by properly combining in sequence the above geometrical transformations and carefully tuning their parameters.

3.3. Insertion of lesions

Another way to expand the range of images is the artificial insertion of lesions within the reference digital phantoms, by means of a replacement of tissue at voxel level. In Fig. 7, we have reported the CC view images calculated after the inclusion of realistic lesions, which can be observed in mammograms with anomalies. As an example, Fig. 7a illustrates how the image of the reference phantom #1 appears after the introduction, in the lower-outer quadrant, of a mass with well-defined margins. This mass, which has a volume of 220 mm^3 and an average diameter of 7.2 mm, can be representative of a cyst, a lump, or in general a benign lesion. The case of a malignant lesion is illustrated in Fig. 7b, with the appearance of a spiculated region characterized by sharp lines radiating from its margin. This is created by inserting again in the lower-outer quadrant a 4 mm sized mass with spicules with length varying from 1 to 6 mm. Another example of anomaly is represented by calcification clusters, like the one simulated in Fig. 7c, where a group of small white spots clearly emerge in the image, due to the very high density of these localized regions with respect to the surrounding tissues. In particular, four lobular calcifications are inserted in the upper-outer quadrant, with volume varying from 1.7 to 3.4 mm^3.

The digital model of the different types of lesions can be generated by exploiting the VICTRE pipeline, which includes both a breast mass generation software [40] and a calcification cluster generation algorithm. This approach has been followed for the creation of the lesions shown in Fig. 7a, b and 7c. Alternatively, it is possible to use the MaX-IMA Breast Lesions Models Database, which provides lesion models with realistic shape, obtained from segmentation of CT and tomosynthesis images as well as from mathematical algorithms [41,42]. By varying size, shape and position of the lesions, several images can be generated, contributing to the population of datasets with different pathology subtypes.

Tubular calcifications appearing as linear or rod-like calcium deposits [43] can also be added to the phantom after a proper segmentation of its blood vessels and ducts. To facilitate the segmentation process, we apply the multiscale vessel enhancement filter, developed by Frangi et al. [44], to the trivariate B-spline solid introduced in Sub-section 2.1, analysing its multiscale second-order local structure (Hessian matrix). Using the Vascular Modelling Toolkit (VMTK) software [45,46], a tool widely adopted for the geometric analysis and

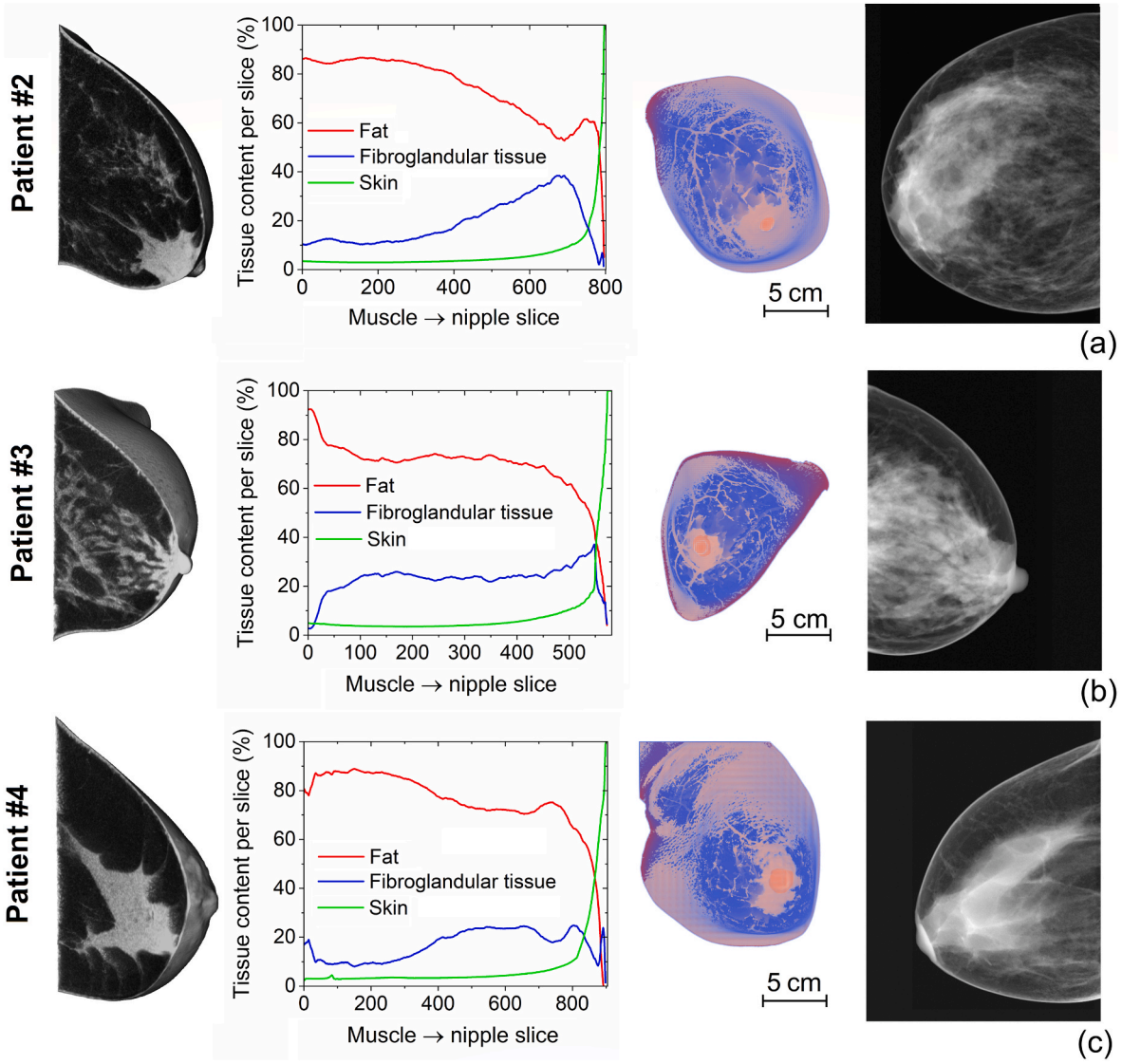

Fig. 5. Visualization of the results obtained from BCT images acquired on patients #2, #3 and #4. On the left: original BCT images compacted in 3D objects. In the centre: percentages of main tissues per each coronal slice from muscle to nipple, and reconstructed reference phantoms in coronal view. On the right: synthetic mammograms calculated in CC view.

reconstruction of tubular structures in medical images and *in silico* testing [47], we define a vesselness 3D function at different scales s, positive outside the vessel-like structure and negative inside it, namely:

$$V(s) = \left[1 - \exp\left(-\frac{R_1^2}{2\alpha^2}\right)\right] \exp\left(-\frac{R_2^2}{2\beta^2}\right) \left[1 - \exp\left(-\frac{S^2}{2\chi^2}\right)\right]. \quad (10)$$

In (10) R_1, R_2 and S are three measures, which are introduced to distinguish between plate- and line-like structures (R_1), to discriminate blob-like structures (R_2), and to quantify grey-level contrast (S), for differentiating the background from the relevant structures. Parameters α, β and χ are thresholds that control the sensitivity of the filter to the measures R_1, R_2 and S, respectively; here, we select $\alpha = 0.5$, $\beta = 0.5$ and $\chi = 7$. We also define the minimum (s_{min}) and maximum (s_{max}) scales of the structures of interest, which can be chosen so that they cover the entire range of vessel and duct widths; here, we fix s_{min} to 0.7 and s_{max} to 2. Then, we integrate the vesselness measure provided by the filter response at different scales between s_{min} and s_{max} to obtain a probability-like estimate of vesselness.

To introduce tubular calcifications in a specific breast region, we assign to all the phantom voxels belonging to this region and with vesselness value within a specified interval the material properties of calcification. As an example, Fig. 7d shows a mammogram where vascular calcifications are inserted in the upper-outer and lower-outer quadrants, in proximity to the skin, considering a range of vesselness from −0.4 to −0.1. With this choice, the introduced calcifications do not replace the entire vessel volume, guaranteeing the presence of a lumen inside. By tuning the extension of the vesselness interval, we can vary the calcification status.

3.4. Quality assessment of the synthesized mammograms at texture level

The quality of the synthesized mammograms is evaluated in comparison to real ones by calculating a series of metrics, which can provide a quantitative measure of texture similarity. The analysis is performed on regions of interest (ROIs) with 300 × 300 px size, mainly containing a specific type of tissue (adipose or fibroglandular). The real ROIs are extracted from mammograms acquired with Siemens scanners, belonging to the Vietnamese dataset of digital mammography (VinDr-Mammo) [48–50].

We estimate the self-similarity of texture at different scales by means of the fractal dimension (FD), derived from both box-counting method

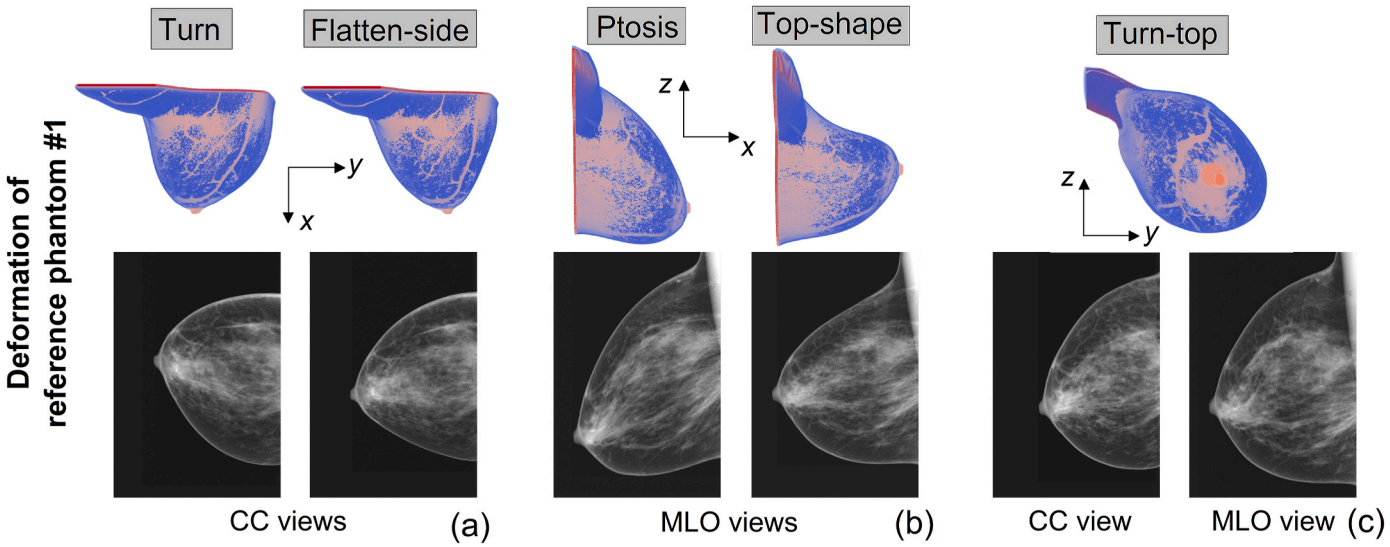

Fig. 6. Examples of breast phantom deformations (top) with associated synthetic mammograms (bottom): (a) turn and flatten-side deformations with relative CC images; (b) ptosis and top-shape deformations with relative MLO images; (c) turn-top deformation with relative CC and MLO images. The geometric transformations are applied to the reference breast phantom from patient #1.

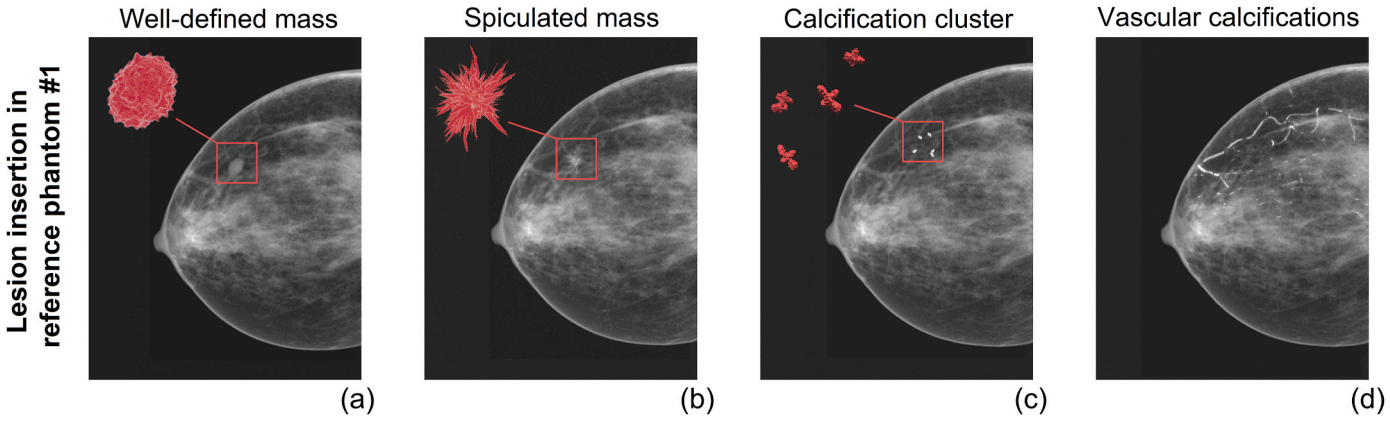

Fig. 7. Examples of synthetic mammograms in CC view generated from the reference phantom from patient #1 by including artificial lesions of different type: (a) round mass with well-defined margins; (b) spiculated mass; (c) cluster of calcifications; (d) vascular calcifications.

and FFT-based power spectrum analysis, for the latter FD $= (8 - \beta)/2$, where β is the average log-log slope [51–54]. In parallel, we evaluate the entropy within the extracted ROIs, to measure the texture complexity by quantifying its degree of disorder/uniformity [55]. For the above metrics, greater texture similarity between synthetic and real ROIs is indicated by closer values. Moreover, the synthetic ROIs are directly compared with those extracted from real mammograms by calculating the Feature Similarity (FSIM) index, which enables us to measure similarity by means of phase congruency and gradient magnitude feature maps [56]. It ranges from 0 to 1, where 1 indicates perfect similarity. To provide a quantitative comparison with well-established *in silico* approaches, the analysis is also performed on ROIs extracted from mammograms generated by using the entire VICTRE pipeline, including phantom creation with a voxel resolution of 50 μm, thus compatible with the resolution of mammography.

All the metric values are reported in Table 2, considering two sets of ROIs with a prevalence of fibroglandular or adipose tissue. For both the two compared methods for generating synthetic images (i.e. our proposed approach using patient–based phantoms and the one exploiting the entire VICTRE pipeline), the greatest similarity to the real ROI is achieved for the fibroglandular tissue ROIs. For the case of adipose tissue, better scores are obtained for the ROI generated with the patient–based phantom approach, with a higher value of FSIM, and values of FDs and entropy closer to the ones evaluated for the real ROI.

Finally, a short visual grading analysis (VGA) is performed by the two co-authors from the Dutch Expert Centre for Screening (LRCB) in the Netherlands, both experts in radiology with a focus on mammography. The image quality criteria adopted for the assessment of the realism of the synthesized mammograms, and the relative scores, are summarized in Table 3, distinguishing among anatomical structures and tissues. They point out that the spatial distribution of fibroglandular and adipose tissues throughout all the breast shape is sufficiently realistic, the greyscale of fibroglandular tissue and soft tissue lesions are well reproduced, and the skin line and the nipple are adequately constructed. However, the obtained images are easily distinguishable as synthetic, due to the low resolution inherited from the BCT images. As a consequence, the Cooper's ligaments are not clearly visible, the vessels contain gaps and cannot be seen in dense areas, and the ducts are not sharply depicted. Also the representation of soft tissue lesion margins and calcifications suffers from the low resolution of the images, needing to be improved.

Table 2
Quality assessment of the synthesized mammograms at texture level, performed by calculating different metrics on ROIs extracted from clinical images and from the images generated with our patient-based phantom approach and the entire VICTRE pipeline.

Tissue	ROI		Box-counting FD	FFT-based FD	Entropy	FSIM
Fibroglandular	Real	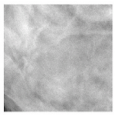	1.92 ± 0.44	2.66	6.39	/
	Patient-based phantom		2.07 ± 0.40	2.68	6.62	0.71
	VICTRE-based phantom	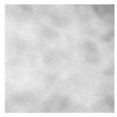	2.09 ± 0.46	2.83	5.95	0.71
Adipose	Real	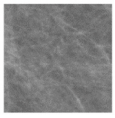	1.93 ± 0.41	2.85	5.38	/
	Patient-based phantom	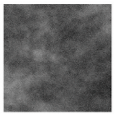	2.16 ± 0.34	2.94	6.13	0.69
	VICTRE-based phantom	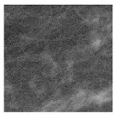	2.16 ± 0.32	3.10	6.33	0.61

3.5. Advancements, limitations and future directions

The proposed methodology has been demonstrated to be suitable for the generation of multiple synthetic mammograms, reproducing anatomical structures and textures with an adequate level of realism. The possibility of including different types of lesions directly in the phantoms enables us to easily perform data augmentation, in view of AI application for anomaly detection, providing an instrument that can support training, validation, generalisability and explainability tasks. Moreover, the applied geometrical transformations mimic the common deformities that can be observed in breast shape, representing a step forward with respect to the use of conventional data augmentation techniques, based on translation, rotation, scaling, flipping or resizing [57].

Another important achievement is the possibility of generating mammograms not only in CC view, but also in MLO view, with the introduction of the pectoralis muscle forming a V shape, typically well evident when the image is acquired after positioning and compressing the breast at 45°. Moreover, thanks to the use of a multiscale vessel enhancement filter, it becomes possible to easily include in tubular structures, like vessels and ducts, distributed calcifications. An additional advantage is that the synthetic mammogram dataset can be further expanded by using Neural Style Transfer methods, which can allow us to replicate the style from various mammography scanner vendors, strongly differing in terms of sharpness, contrast, texture appearance and overall grey level distribution [58–60].

In comparison to other *in silico* approaches, like the one exploiting the entire VICTRE pipeline [21], ours has the limitation that the phantoms are originated from medical images, thus inherit possible artefacts, noise, low contrast, and low resolution of the source data. In the specific case of phantoms obtained from BCT images, large-scale features are well reproduced, but fine details associated with the linear structures (i.e. ductal network, blood vessels and Cooper's ligaments) are not accurately depicted, as can be done with VICTRE. Anyway, with our approach, and, in general, with patient-based phantom reconstruction, it is possible to obtain more realistic representations of the parenchyma, and of the boundaries between fibroglandular and adipose tissues [61]. As pointed out by the VGA in Table 3, the generated phantoms lead to synthetic mammograms where the spatial distribution of fibroglandular and adipose regions is appropriately depicted throughout all the breast shape. In particular, there is an increase in density of tissue pattern from the pectoral side to the nipple, difficult to reproduce with the phantoms created with VICTRE, which leads to more random distributions of fibroglandular regions. Nevertheless, patient-based approaches are more computationally expensive and have the drawback that the number of independent phantoms that can be produced depends on the clinical data available, differently from the approaches using mathematical methodologies [21,62,63].

Another limitation of the developed methodology is that the obtained images have a resolution comparable to the lowest one of real digital mammograms, which have a pixel size typically ranging between 50 and 100 μm [64]. The reason is that the phantom has been derived from BCT images with a lower spatial resolution (around 270 μm); thus, the anatomical detail content in the generated synthetic mammograms results to be smaller than the one detectable in current mammography.

A possible solution for improving the final resolution of the calculated x-ray projections is to use, as an input of the phantom generation process, images acquired with the most recent cone-beam BCT scanners, with a spatial resolution of up to 100 μm per pixel in all the three dimensions, and thus comparable to the resolution of digital

Table 3
Quality assessment of the synthesized mammograms, performed by means of visual grading analysis (VGA).

Anatomical structure/ Tissue	Image quality criteria	Rating scale
Adipose/fibroglandular	Appropriate construction of spatial distribution of adipose and fibroglandular tissues throughout the breast shape	**Good:** the spatial distribution of adipose and fibroglandular tissues is appropriately depicted throughout all the breast shape, with a realistic increase in density of tissue pattern from the pectoral side to the nipple.
Adipose/fibroglandular	Appropriate depiction of adipose and fibroglandular tissue texture	**Fair:** it is possible to perceive differences in breast tissue due to texture variation. However, the synthetic images have much lower resolution than the real ones leading to correlation between pixel values. Moreover, due to the noise texture, the adipose tissue is not sufficiently black.
Fibroglandular	Appropriate depiction of fibroglandular tissue greyscale	**Good:** the greyscale of fibroglandular tissue is sufficiently realistic.
Connective tissue, vessels and ducts	Sharp depiction of Cooper's ligaments, vessels and ducts	**Fair:** the Cooper's ligaments are not clearly visible, the vessels are constructed with gaps and cannot be seen in dense areas, and the ducts are not sharply depicted.
Pectoralis muscle	Appropriate depiction of the pectoralis muscle, when present	**Medium:** in MLO view the muscle is depicted with a correct angle and greyscale level, but is somewhat artificial from an anatomical point of view.
Skin	Appropriate depiction of skin line with respect to background and breast shape	**Good:** The skin line shows some white band artefacts, reproducing skin line artefacts that can be seen in real mammography images.
Nipple	Visibility of nipple	**Good:** The nipple is visible in most cases. In some cases the nipple is not visible, but this can also occur incidentally in real mammography.
Soft tissue lesions	Visualization of soft tissue lesions with a different density with respect to the surrounding tissue	**Good:** the greyscale level of the soft tissue lesions seems realistic.
Soft tissue lesions	Visibility of soft tissue lesion morphology	**Fair:** the soft tissue lesion morphology is difficult to appreciate due to the low resolution of the images.
Soft tissue lesions	Sharp depiction of soft tissue lesion margins	**Fair:** due to the low resolution, soft tissue lesion margins are difficult to interpret.
Calcifications	Visualization of calcifications with a different density with respect to the surrounding tissue	**Medium:** The density of vascular calcifications with respect to the surrounding tissue seems appropriate. The calcifications clusters seems too bright, making their depiction not sufficiently realistic.
Calcifications	Visibility of calcification morphology	**Fair:** The visibility of calcifications suffers from the low resolution of the images, making their depiction not sufficiently realistic.

mammography [65]. Another approach is to leverage machine-learning models to generate super-resolution breast phantoms, but this requires the availability of high-resolution breast specimen images, like the ones obtained with synchrotron CT systems, for the proper training of the algorithms [66]. As an alternative solution, super-resolution techniques based on convolutional neural networks can be directly applied to the low-resolution synthetic mammograms, making them appear sharper and more detailed, while preserving their content and anatomical features [67].

4. Conclusion

In this work, we have proposed a methodology that, starting from sets of dedicated BCT images acquired on different patients, enables us to create highly realistic digital phantoms, to be used for generating synthetic mammograms. Exploiting trivariate tensor product B-splines and morphological operations, we perform tissue segmentation, distinguishing among fibroglandular, fat and skin tissues, and obtain voxel-based structures having spatial resolution nearly compatible with digital mammography. The generated phantoms are then used as input for the biomechanical compression and x-ray imaging simulation process implemented in the VICTRE pipeline, which allows us to obtain synthetic mammograms in "for presentation" form.

Data augmentation is carried out introducing shape modifications to the reconstructed phantoms, through the application of geometric transformations that replicate common anatomical deformities. To better reflect the variability observed in real-world clinical cases, we also introduce different types of lesions, including round or spiculated masses, tubular calcifications or clusters of microcalcifications. This approach offers a significant advantage, as it enables the generation, from a single BCT scan, of multiple sufficiently realistic synthetic mammograms, differing in breast profile and lesion features. The number of cases can be indeed increased if the available BCT scans cover the different types of breast composition, from almost fatty to extremely dense. Such flexibility can be leveraged to produce synthetic databases, which can be effectively used to train and benchmark AI models, thereby enhancing their robustness and generalisability in breast diagnostic imaging.

CRediT authorship contribution statement

Martina Oria: Writing – review & editing, Visualization, Validation, Software, Methodology, Investigation, Formal analysis, Data curation, Conceptualization. **Riccardo Ferrero:** Writing – review & editing, Visualization, Validation, Software, Methodology, Investigation, Formal analysis, Data curation, Conceptualization. **Chiara Andreis:** Writing – review & editing, Visualization, Software, Methodology, Investigation, Formal analysis. **Marta Vicentini:** Writing – review & editing, Visualization, Validation, Investigation. **Ruben van Engen:** Writing – review & editing, Visualization, Validation, Resources, Investigation, Conceptualization. **Carlijn Roozemond:** Writing – review & editing, Visualization, Validation, Resources, Investigation. **Paola Lamberti:** Writing – review & editing, Supervision, Software, Methodology. **Sara Remogna:** Writing – review & editing, Supervision, Software, Methodology. **Alessandra Manzin:** Writing – review & editing, Writing – original draft, Visualization, Validation, Supervision, Software, Resources, Project administration, Methodology, Investigation, Funding acquisition, Formal analysis, Conceptualization.

Ethics statement

The authors declare that there is no ethics approval needed for the current study. The source of the used set of dedicated BCT images, acquired on one patient, is a previous ethics board-approved patient trial (see Ref. [25]), for which all the involved subjects provided written informed consent.

Declaration of competing interest

None to be declared.

Acknowledgements

This work is supported by Project 22HLT05 MAIBAI, which has received funding from the European Partnership on Metrology, co-financed from the European Union's Horizon Europe Research and Innovation Programme and by the Participating States.

The authors are grateful to Prof. Ioannis Sechopoulos, professor at Radboud University Medical Center, Nijmegen, Netherlands, and scientific advisor at LRCB, for the provision of the BCT images used in this work.

References

[1] W. Kainz, et al., Advances in computational human phantoms and their applications in biomedical engineering – a topical review, IEEE Trans. Radiat. Plasma Med. Sci. 3 (1) (2019) 1–23.
[2] E. Abadi, et al., Virtual clinical trials in medical imaging: a review, J. Med. Imaging 7 (4) (2020) 042805.
[3] C. Choi, et al., Body-size-dependent phantom library constructed from ICRP mesh-type reference computational phantoms, Phys. Med. Biol. 65 (12) (2020) 125014.
[4] A. Akhavanallaf, et al., An update on computational anthropomorphic anatomical models, Digital Health 8 (2022) 1–12.
[5] S. Manohar, I. Sechopoulos, M.A. Anastasio, L. Maier-Hein, R. Gupta, Super phantoms: advanced models for testing medical imaging technologies, Commun. Eng. 3 (2024) 73.
[6] C. Sainz Martinez, M. Bach Cuadra, J. Jorge, BigBrain-MR: a new digital phantom with anatomically-realistic magnetic resonance properties at 100-μm resolution for magnetic resonance methods development, Neuroimage 273 (2023) 120074.
[7] Y. Wu, et al., Realistic digital phantoms for prostate ultrasound and photoacoustic imaging. Medical Imaging 2024: Ultrasonic Imaging and Tomography, Proc. SPIE 12932, 2024, https://doi.org/10.1117/12.3006921, 129321D.
[8] A. Sarno, et al., Dataset of patient-derived digital breast phantoms for in silico studies in breast computed tomography, digital breast tomosynthesis, and digital mammography, Med. Phys. 48 (5) (2021) 2682–2693.
[9] K. Bliznakova, The advent of anthropomorphic three-dimensional breast phantoms for X-ray imaging, Phys. Med. 79 (2020) 145–161.
[10] S.J. Glick, L.C. Ikejimba, Advances in digital and physical anthropomorphic breast phantoms for x-ray imaging, Med. Phys. 45 (10) (2018) e870–e884.
[11] D. M Mahr, R. Bhargava, M.F. Insana, Three-dimensional in silico breast phantoms for multimodal image simulations, IEEE Trans. Med. Imag. 31 (3) (2011) 689–697.
[12] L.M. Carter, J.C. Ocampo Ramos, W.E. Bolch, J.S. Lewis, A.L. Kesner, Technical note: patient-Morphed mesh-type phantoms to support personalized nuclear medicine dosimetry – a proof of concept study, Med. Phys. 48 (4) (2021) 2018–2026.
[13] I. Androulakis, K. Sumser, M.N.D. Machielse, L. Koppert, A. Jager, R. Nout, M. Franckena, G. C van Rhoon, S. Curto, Patient-derived breast model repository, a tool for hyperthermia treatment planning and applicator design, Int. J. Hyperther. 39 (1) (2022) 1213–1221.
[14] S. Singh, R. Melnik, Thermal ablation of biological tissues in disease treatment: a review of computational models and future directions, Electromagn. Biol. Med. 39 (2) (2020) 49–88.
[15] B. D Killeen, S. Min Cho, M. Armand, R.H. Taylor, M. Unberath, In silico simulation: a key enabling technology for next-generation intelligent surgical systems, Prog. Biomed. Eng. 5 (3) (2023) 032001.
[16] E.L. Carniel, I. Toniolo, C.G. Fontanella, Computational biomechanics: in-silico tools for the investigation of surgical procedures and devices, Bioengineering 7 (2) (2020) 48.
[17] Computational anatomical animal models: methodological developments and research applications, Published by Institute of Physics, in: H. Zaidi (Ed.), IPEM-IOP Series in Physics and Engineering in Medicine and Biology, December 2018.
[18] T. Xie, J. Seo Park, W. Zhuo, H. Zaidi, Development of a nonhuman primate computational phantom for radiation dosimetry, Med. Phys. 47 (2) (2020) 736–744.
[19] M. Vicentini, M. Vassallo, R. Ferrero, I. Androulakis, A. Manzin, In silico evaluation of adverse eddy current effects in preclinical tests of magnetic hyperthermia, Comput. Methods Progr. Biomed. 223 (2022) 106975.
[20] M. Vicentini, R. Ferrero, A. Manzin, In silico experiments to explore the heating efficiency of magnetic nanoparticles in hyperthermia preclinical tests, Adv. Theory Simul. 6 (7) (2023) 2300234.
[21] A. Badal, D. Sharma, C.G. Graff, R. Zeng, A. Badano, Mammography and breast tomosynthesis simulator for virtual clinical trials, Comput. Phys. Commun. 261 (2021) 107779.
[22] G.M. Sturgeon, S. Park, W.P. Segars, J.Y. Lo, Synthetic breast phantoms from patient based eigenbreasts, Med. Phys. 44 (12) (2017) 6270–6279.
[23] C.M.L. Hsu, M.L. Palmeri, W.P. Segars, A.I. Veress, J.T. Dobbins III, Generation of a suite of 3D computer-generated breast phantoms from a limited set of human subject data, Med. Phys. 40 (4) (2013) 043703.
[24] L.A. Piegl, W. Tiller, The NURBS Book, Springer Berlin, Heidelberg, 1997.
[25] M. Caballo, J.M. Boone, R. Mann, I. Sechopoulos, An unsupervised automatic segmentation algorithm for breast tissue classification of dedicated breast computed tomography images, Med. Phys. 45 (6) (2018) 2542–2559.
[26] S.-Y. Huang, J.M. Boone, K. Yang, A.L.C. Kwan, N.J. Packard, The effect of skin thickness determined using breast CT on mammographic dosimetry, Med. Phys. 35 (4) (2008) 1199–1206.
[27] D.T. Chen, I.A. Kakadiaris, M.J. Miller, R.B. Loftin, C. Patrick, Modeling for plastic and reconstructive breast surgery, in: S.L. Delp, A.M. Di Goia, B. Jaramaz (Eds.), Medical Image Computing and Computer-Assisted Intervention – MICCAI 2000. Lecture Notes in Computer Science, vol. 1935, Springer, Berlin, Heidelberg, 2000, https://doi.org/10.1007/978-3-540-40899-4_108.
[28] S.A. Maas, B.J. Ellis, G.A. Ateshian, J.A. Weiss, FEBio: finite elements for biomechanics, J. Biomech. Eng. 134 (1) (2012) 011005.
[29] https://www.volparahealth.com/app/uploads/2021/09/Volumetric-Breast-Density-Scale-Digital.pdf.
[30] D.A. Spak, J.S. Plaxco, L. Santiago, M.J. Dryden, B.E. Dogan, BI-RADS® fifth edition: a summary of changes, diagn, Interv. Imaging 98 (3) (2017) 179–190.
[31] J. Boone, T. Fewell, R. Jennings, X-ray transmission formula for antiscatter grids, Med. Phys. 24 (1997) 1863–1874.
[32] S. Vrbaški, L.M. Arana Peña, L. Brombal, S. Donato, Angelo Taibi, A. Contillo, R. Longo, Characterization of breast tissues in density and effective atomic number basis via spectral X-ray computed tomography, Phys. Med. Biol. 68 (2023) 145019.
[33] J.S. Camilleri, et al., Review of thermal and physiological properties of human breast tissue, Sensors 22 (10) (2022) 3894.
[34] Md Monirujjaman, L. Martin, C. Stretch, V.C. Mazurak, Adipose tissue radiodensity in chronic diseases: a literature review of the applied methodologies, Immunometabolism 3 (4) (2021) e210033.
[35] H. Jung, Basic physical principles and clinical applications of computed tomography, Progr. Med. Phys. 32 (1) (2021) 1–17.
[36] N. Perry, M. Broeders, C. de Wolf, S. Törnberg, R. Holland and L. von Karsa, European Guidelines for Quality Assurance in Breast Cancer Screening and Diagnosis. fourth ed. – Supplements, https://op.europa.eu/en/publication-detail/-/publication/4e74ee9b-df80-4c91-a5fb-85efb0fdda2b..
[37] A.A. Gemici, E. Arıbal, A.N. Özaydın, S.Ö. Gürdal, B. Özçınar, N. Cabioğlu, V. Özmen, Comparison of qualitative and volumetric assessments of breast density and analyses of breast compression parameters and breast volume of women in bahcesehir mammography screening project, Eur. J. Breast Health 16 (2) (2020) 110–116.
[38] A.E. Burgess, H. Kang, Incomplete skin representation in digital mammograms, Med. Phys. 31 (10) (2004) 2834–2838.
[39] T.L. Pope Jr., M.E. Read, T. Medsker, A.J. Buschi, A.N. Brenbridge, Breast skin thickness: normal range and causes of thickening shown on film-screen mammography, J. Can. Assoc. Radiol. 35 (4) (1984) 365–368.
[40] L. de Sisternes, J.G. Brankov, A.M. Zysk, R.A. Schmidt, R.M. Nishikawa, M. N. Wernick, A computational model to generate simulated three-dimensional breast masses, Med. Phys. 42 (2) (2015) 1098–1118.
[41] K. Bliznakova, et al., Development of breast lesions models database, Phys. Med. 64 (2019) 293–303.
[42] N. Dukov, K. Bliznakova, F. Feradov, I. Buliev, H. Bosmans, G. Mettivier, P. Russo, L. Cockmartin, Z. Bliznakov, Models of breast lesions based on three-dimensional X-ray breast images, Phys. Med. 57 (2019) 80–87.
[43] L. Wilkinson, V. Thomas, N. Sharma, Microcalcification on mammography: approaches to interpretation and biopsy, Br. J. Radiol. 90 (1069) (2017) 20160594.
[44] A.F. Frangi, W.J. Niessen, K.L. Vincken, M.A. Viergever, Multiscale vessel enhancement filtering, in: W.M. Wells, A. Colchester, S. Delp (Eds.), Medical Image Computing and Computer-Assisted Intervention – MICCAI'98, Springer, Berlin, Heidelberg, 1998, pp. 130–137, https://doi.org/10.1007/BFb0056195.
[45] vmtk - the vascular modelling toolkit, available online: http://www.vmtk.org/.
[46] L. Antiga, M. Piccinelli, L. Botti, B. Ene-Iordache, A. Remuzzi, D.A. Steinman, An image-based modeling framework for patient-specific computational hemodynamics, Med. Biol. Eng. Comput. 46 (2008) 1097–1112.
[47] M. Vicentini, R. Ferrero, A. Manzin, Modelling of magnetic bead transport in a microvascular network, J. Magn. Magn Mater. 513 (2020) 167234.
[48] H.H. Pham, H.T. Nguyen, H.Q. Nguyen, VinDr-Mammo: a large-scale benchmark dataset for computer-aided detection and diagnosis in full-field digital mammography, PhysioNet (2022), https://doi.org/10.13026/br2v-7517 [Data set], version 1.0.0.
[49] A. Goldberger, et al., PhysioBank, PhysioToolkit, and PhysioNet: components of a new research resource for complex physiologic signals, Circulation 101 (23) (2000) e215–e220.
[50] H.T. Nguyen, et al., VinDr-Mammo: a large-scale benchmark dataset for computer-aided diagnosis in full-field digital mammography, Sci. Data 10 (2023) 277.
[51] K. Bliznakova, S. Suryanarayanan, A. Karellas, N. Pallikarakis, Evaluation of an improved algorithm for producing realistic 3D breast software phantoms: application for mammography, Med. Phys 37 (11) (2010) 5604–5617.
[52] P. Elangovan, et al., Design and validation of realistic breast models for use in multiple alternative forced choice virtual clinical trials, Phys. Med. Biol. 62 (7) (2017) 2778–2794.
[53] J. Wang, Y. Liu, A. Hu, S. Wei, T. Wu, J. Li, R. Qiu, Image simulation and realism evaluation for mammography and tomosynthesis based on the detailed breast phantom, Radiat. Phys. Chem. 213 (2023) 111241.
[54] D. Kontos, P.R. Bakic, A.-K. Carton, A.B. Troxel, E.F. Conant, A.D.A. Maidment, Parenchymal texture analysis in digital breast tomosynthesis for breast cancer risk estimation: a preliminary study, Acad. Radiol. 16 (3) (2009) 283–298.
[55] R.C. Gonzalez, R.E. Woods, S.L. Eddins, Digital Image Processing Using MATLAB, Prentice Hall, New Jersey, 2003. Chapter 11.
[56] L. Zhang, L. Zhang, X. Mou, D. Zhang, FSIM: a feature similarity index for image quality assessment, IEEE Trans. Image Process. 20 (8) (2011) 2378–2386.

[57] P. Oza, P. Sharma, S. Patel, F. Adedoyin, A. Bruno, Image augmentation techniques for mammogram analysis, J. Imaging 8 (5) (2022) 141.
[58] S. Wang, et al., mr2 NST: multi-Resolution and multi-reference neural style transfer for mammography, in: Proceedings of PRIME 2020: International Workshop on PRedictive Intelligence In MEdicine, Lecture Notes in Computer Science, 12329, 2020, pp. 169–177.
[59] Z. Li, et al., Domain generalization for mammography detection via multi-style and multi-view contrastive learning, in: Proceedings of MICCAI 2021: International Conference on Medical Image Computing and Computer-Assisted Intervention, Lecture Notes in Computer Science, 12907, 2021, pp. 98–108.
[60] M. Oria, R. Ferrero, M. Vicentini, A. Manzin, Generation of synthetic images for mammography via neural networks based methods, Phys. Med. 125 (1) (2024) 103596.
[61] C. Fedon, M. Caballo, E. García, O. Diaz, J.M. Boone, D.R. Dance, I. Sechopoulos, Fibroglandular tissue distribution in the breast during mammography and tomosynthesis based on breast CT data: a patient-based characterization of the breast parenchyma, Med. Phys. 48 (3) (2021) 1436–1447.
[62] K. Bliznakova, Z. Bliznakov, V. Bravou, Z. Kolitsi, N. Pallikarakis, A three-dimensional breast software phantom for mammography simulation, Phys. Med. Biol. 48 (22) (2003) 3699–3719.
[63] D.D. Pokrajac, A.D. Maidment, P.R. Bakic, Optimized generation of high resolution breast anthropomorphic software phantoms, Med. Phys. 39 (4) (2012) 2290–2302.
[64] W. Huda, R. Brad Abrahams, X-Ray-Based medical imaging and resolution, Am. J. Roentgenol. 204 (4) (2015) W393–W397.
[65] K. Siddall, X. Zhang, A. O'Connell, Emerging clinical applications for cone beam breast CT: changing the breast imaging paradigm, Curr. Breast Cancer Rep. 16 (2024) 134–141.
[66] M. Caballo, C. Fedon, L. Brombal, R. Mann, R. Longo, I. Sechopoulos, Development of 3D patient-based super-resolution digital breast phantoms using machine learning, Phys. Med. Biol. 63 (2018) 225017.
[67] K. Umehara, J. Ota, T. Ishida, Super-Resolution imaging of mammograms based on the super-resolution convolutional neural network, Open J. Med. Imag. 7 (4) (2017) 180–195.